Special Collection

Unravelling the Zn-Cu Interaction during Activation of a Zn-promoted Cu/MgO Model Methanol Catalyst

Lakshmi Pandit,[a, b] Alexey Boubnov,[a, b] Gereon Behrendt,[c] Benjamin Mockenhaupt,[c] Chandra Chowdhury,[b] Jelena Jelic,[b] Anna-Lena Hansen,[d] Erisa Saraçi,[a, b] Erik-Jan Ras,[e] Malte Behrens,[c, f] Felix Studt,[a, b] and Jan-Dierk Grunwaldt*[a, b]

We report on an inverse model Cu/MgO methanol catalyst modified with 5% zinc oxide at the Cu surface to element-specifically probe the interplay of metallic copper and zinc oxide during reductive activation. The structure of copper and zinc was unraveled by *in situ* X-ray diffraction (XRD) and *in situ* X-ray absorption spectroscopy (XAS) supported by theoretical modelling of the extended X-ray absorption fine structure and X-ray absorption near-edge structure spectra. Temperature-programmed reduction in H_2 during *in situ* XAS showed that copper was reduced starting at 145 °C. With increasing reduction temperature, zinc underwent first a geometrical change in its structure, followed by reduction. The reduced zinc species were identified as surface alloy sites, which coexisted from 200 °C to 340 °C with ZnO species at the copper surface. At 400 °C Zn–Cu bulk-alloyed particles were formed. According to *in situ* XRD and *in situ* XAS, about half of the ZnO was not fully reduced, which can be explained by a lack of contact with copper. Our experimental results were further substantiated by density functional theory calculations, which verified that ZnO with neighboring Cu atoms reduced more easily. By combining these results, the distribution, phase and oxidation state of Zn species on Cu were estimated for the activated state of this model catalyst. This insight into the interplay of Cu and Zn forms the basis for deeper understanding the active sites during methanol synthesis.

1. Introduction

The development of Cu-based catalysts for methanol synthesis is particularly attractive after a renewed interest in methanol has been generated as an energy storage molecule.[1] An important aspect of the Power-to-Liquid concept is the efficient functioning of these catalysts in dynamic conditions owing to the fluctuating nature of renewable energy sources, in this case, hydrogen.[2] Currently, methanol is synthesized by hydrogenation of CO and CO_2 using the $Cu/ZnO/Al_2O_3$ catalyst at temperatures of 200–300 °C and pressures of 50–100 bar.[1b,3]

The reaction rates in terms of turnover frequencies (TOF) over $Cu/ZnO/Al_2O_3$ catalysts are traced back to various reasons, such as a high surface area and small particle size of Cu, optimized morphologies, presence of defects such as micro-strains, kinks or twin boundaries in the Cu microstructure.[4] In fact, catalysts with Zn-decorated Cu surfaces showed greater activity than catalysts without any Zn-decoration.[5] $Zn(O)_x$ is known to have two important functions: (1) structural: as a physical spacer during synthesis for a uniform and high dispersion of Cu nanoparticles,[6] and for protecting Cu from sintering during reaction conditions.[7] (2) promoter: $Zn(O)_x$ is speculated to act as electronic promoter for Cu including its interface.[8] The value of x ($0 < x < 1$) determines the degree of reduction of the Zn species. One hypothesis is that the promotional effects are due to enrichment of $Zn(O)_x$ species on the copper surface.[9] Reduced Zn-species or even a surface alloy with copper has been also suggested as active species.[10] Furthermore, there is a strong metal-support interaction (SMSI) of Cu particles with the reduced $Zn(O)_x$-surface. This may lead to dynamic restructuring, morphological changes and surface

[a] L. Pandit, Dr. A. Boubnov, Dr. E. Saraçi, Prof. F. Studt, Prof. J.-D. Grunwaldt
Institute for Chemical Technology and Polymer Chemistry (ITCP)
Karlsruhe Institute of Technology (KIT)
76131 Karlsruhe (Germany)
E-mail: grunwaldt@kit.edu
[b] L. Pandit, Dr. A. Boubnov, Dr. C. Chowdhury, Dr. J. Jelic, Dr. E. Saraçi, Prof. F. Studt, Prof. J.-D. Grunwaldt
Institute of Catalysis Research and Technology (IKFT)
Karlsruhe Institute of Technology (KIT)
76344 Eggenstein-Leopoldshafen (Germany)
[c] G. Behrendt, B. Mockenhaupt, Prof. M. Behrens
Faculty of Chemistry and Center for Nanointegration Duisburg-Essen (CENIDE)
University of Duisburg-Essen
45141 Essen (Germany)
[d] Dr. A.-L. Hansen
Institute of Applied Materials (IAM)
Karlsruhe Institute of Technology (KIT)
76344 Eggenstein-Leopoldshafen (Germany)
[e] Dr. E.-J. Ras
Avantium Technologies B.V.
1014 BV Amsterdam (The Netherlands)
[f] Prof. M. Behrens
Institute of Inorganic Chemistry
Christian-Albrechts University Kiel
24118 Kiel (Germany)

Supporting information for this article is available on the WWW under https://doi.org/10.1002/cctc.202100692

Special Collection

This publication is part of a joint Special Collection with ChemElectroChem on "Catalysts and Reactors under Dynamic Conditions for Energy Storage and Conversion (DynaKat)". Please check our homepage for more articles in the collection.

alloying due to the reversible oxidation states of Zn and Cu, which depend on the reduction potential and syngas composition,[2,11] underlining that *x* is variable and depends on the reaction conditions. Under dynamic conditions in particular, this spontaneous re-adjustment is believed to influence the intrinsic activity of the methanol catalyst, e.g. by forming an active zinc formate/Cu metal bi-functional catalyst or active/inactive bulk brass.[10,12] Therefore, the role of Zn species in Cu-based methanol catalysts is still highly controversial and its ultimate elucidation would be a significant contribution in the area of methanol synthesis and renewable energy storage.

From an academic point of view, several challenges are met in an attempt to study the promotional effects of $Zn(O)_x$ and the synergistic interaction with Cu in the industrial Cu/ZnO/Al_2O_3 catalyst which are at the origin of the controversial discussions in literature. The high ZnO content, required for structural stabilization of Cu nanoparticles in standard methanol catalysts, largely constitutes spectator species along with the promotional role of $Zn(O)_x$. On the other hand, bulk ZnO is able to undergo own reactions independent of Cu, e.g., transformation to formates,[8,10] and can be interpreted as part of a bi-functional catalyst. Since $Zn(O)_x$ has this dual function, it is necessary to separate its role as physical support in order to study specifically its promotional effects. Hence, an "inverse" model catalyst Cu/MgO:ZnO (referred to as CMZ), containing unreducible MgO as structural stabilizer instead of ZnO for Cu particles and only a low amount of ZnO, specifically interacting with Cu, would be ideal model for investigating the promotional role of Zn species with element-specific methods. Such a catalyst design has been reported previously,[13] where a Cu/MgO (CM) could be modified with ZnO in such a way that it behaved similarly as Cu/ZnO (CZ). Whereas Cu/MgO was only active for CO-hydrogenation, the addition of Zn to Cu/MgO inverted its behavior in CO and CO_2 hydrogenation.

In the present work, we focus on determining the Cu–Zn interaction and the state of $Zn(O)_x$ on an "inverse" model Cu/MgO:ZnO catalyst, by investigating the structure of the calcined and reduced Zn-promoted Cu/MgO catalyst as a basis for structure-activity relationship studies. A catalyst prepared *via* co-precipitation of Cu/MgO followed by impregnation with 5% zinc nitrate and calcination, is reduced with hydrogen under mild and harsher conditions to investigate the interaction between $Zn(O)_x$ and the copper surface. We used transmission electron microscopy (TEM) as well as chemical mapping by energy-dispersive X-ray spectroscopy (EDX) to image the elemental distribution, *in situ* X-ray diffraction (XRD) to track the crystalline phases and *in situ* X-ray absorption spectroscopy (XAS) to study in an element-specific way both crystalline and amorphous copper and zinc species during reduction. Furthermore, density functional theory (DFT) calculations explored the feasibility of ZnO reduction in the presence of Cu. Based on this study, we aim to provide a mechanistic understanding of the formation and nature of Zn sites on a Cu-based methanol catalyst for a better understanding of the Cu–Zn system.

2. Results and Discussion

2.1. $Zn(O)_x$-promoted CuO/MgO catalyst

This study focuses on the $Zn(O)_x$ promotion and its structure in Cu/ZnO catalysts. Hence, a model catalyst that separates the dual function of $Zn(O)_x$ and mainly considers its promotional effects was developed. The mixed-oxide catalyst was obtained by impregnation of the precursor mcguinnessite, $(Cu_{0.7}Mg_{0.3})_2CO_3(OH)_2$ with small amounts of $Zn(NO_3)_2$ and was subsequently calcined to decompose the hydroxycarbonates and nitrates to corresponding oxides, resulting in the CMZ catalyst. An unpromoted CM was also prepared from the same precursor as a reference. AAS analysis of the samples (cf. Table 1) shows that the atomic ratios of the metals were as expected at all stages of the synthesis.

The synthesis parameters were optimized with the aim to achieve a uniform dispersion of Zn on the mcguinnessite precursor. Both catalysts exhibited a relatively high surface area ($>60\ m^2/g$). A particularly high surface area ($114\ m^2/g$) was observed for the CMZ catalyst, most probably due to the addition of $Zn(O)_x$-cluster that form during precursor decomposition in agreement with the study by Zander et. al.[13]

TEM images and EDX analysis of calcined and reduced catalyst were collected to analyze the respective morphology and elemental distribution (Figure 1). The EDX-TEM chemical map of the calcined catalyst shown in Figure 1(a) indicates a rather homogeneous distribution of all three elements Cu, Mg and Zn on the nanoscale, with only a few segregated ZnO particles (green areas). Upon reduction (Figure 1(b)), Cu and Zn stayed well-mixed (mixed orange/green areas) and segregated from MgO (blue areas). This is in line with earlier HR-TEM studies on the CM catalyst,[13] where Cu was observed apart from MgO. The small amount of segregated ZnO nanoparticles (green areas) present in the calcined catalyst did not increase upon reduction. Hence, a large fraction of ZnO remained well distributed. The formation and sintering of the copper particles were also observed in the TEM images of the catalyst after reduction compared to the calcined state, Figures 1(c) and (d). Note that the copper surface area of the catalysts as determined

Table 1. Elemental atomic ratios, BET and N_2O surface area of the precursor, the CM reference and the CMZ calcined catalyst.

Sample	Elemental analysis [at.%][a]			BET surface area	N_2O surface area
	Cu	Mg	Zn	[m^2/g]	[m^2/g]
Mcguinnessite precursor	72.0 ± 0.1	28.0 ± 0.1	–	86	–
CuO/MgO (CM)	72.5 ± 0.1	27.5 ± 0.1	–	64	5
CuO/MgO:Zn (CMZ)	67.7 ± 0.1	26.8 ± 0.1	5.5 ± 0.1	114	11

[a] Determined by atomic absorption spectroscopy.

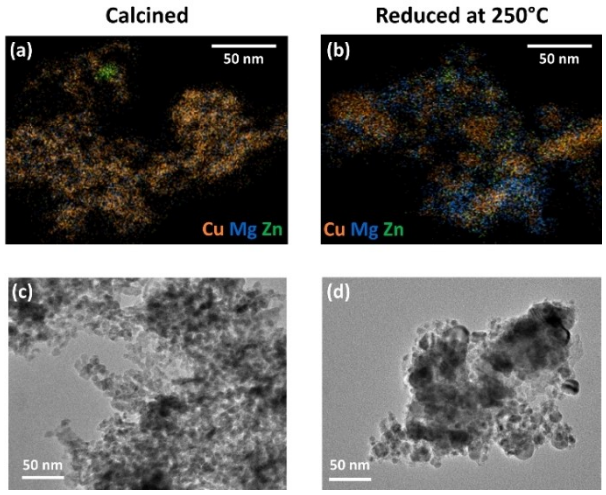

Figure 1. EDX-TEM images of the (a) CMZ calcined and (b) CMZ catalyst reduced at 250 °C. TEM images of (c) CMZ calcined and (d) CMZ after reduction at 250 °C.

by N_2O adsorption on reproduced batches were determined as 5 and 11 m^2/g for the CM and CMZ model catalysts, respectively. The increase with ZnO impregnation can be explained by the new introduction of reduced Zn sites, which are sensitive for N_2O decomposition and add to the contribution of the Cu metal sites, which is in agreement with a previous study.[14]

Surface metal ratios of the calcined and reduced phases were obtained from X-ray photoelectron spectroscopy (XPS). Figure 2 shows that the atomic surface composition (Cu:Mg:Zn = 70.5:24.2:5.5) of the calcined state corresponds closely to its bulk composition (Cu:Mg:Zn = 67.7:26.8:5.5), indicating a homogeneous initial distribution (XP spectra, cf. Fig. S1). After reduction at 250 °C, the surface concentration of Cu decreased and both that of Zn and Mg increased, consistent with the formation of metallic copper particles with oxidized Zn and Mg on the surface. In the X-ray diffraction pattern of the calcined catalyst (cf. next sections), needle-like CuO domains (4.8 × 2.5 × 2.5 nm) and traces of crystalline ZnO of 8.9 nm crystallite size were observed, in agreement with the observed segregated ZnO particles in the EDX mapping. In contrast, no remaining crystalline mcguinnesite precursor or MgO phase could be identified by XRD,[13] indicating the full decomposition of these phases to oxides during calcination. Note that further poorly crystalline oxycarbonate phases may be present in small concentrations, which was previously observed in decomposed hydroxy-carbonate precursors.[15]

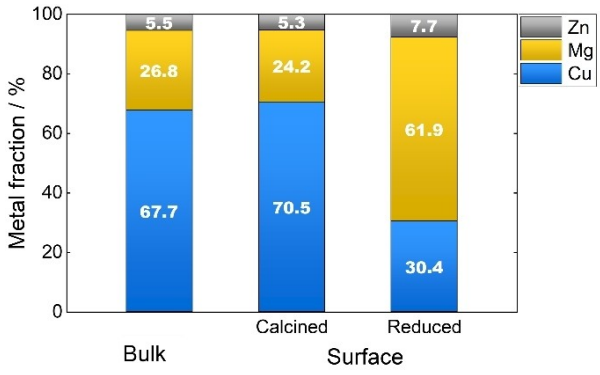

Figure 2. Surface composition of the calcined catalyst and reduced catalyst (reduction at 250 °C, heating rate 5 K/min, dwell time 1 h) determined by XPS (corresponding spectra are shown in Figure S1 in the supporting information).

2.2. Catalytic activity of the Zn-promoted Cu/MgO catalyst compared to the unpromoted Cu/MgO catalyst

The catalytic performance of the Cu/MgO:Zn catalysts (CMZ) was compared with both the unpromoted Cu/MgO (CM) model catalyst as well as a Cu/ZnO (CZ; Cu:Zn = 70:30) reference catalyst. The results are shown in Figure 3. All catalysts were reduced in 5 % H_2 at 275 °C (cf. Experimental section). The ZnO-free Cu/MgO (CM Cu:Zn = 70:30) catalyst only produced significant amounts of methanol from CO but not CO_2-containing gas feeds (Figure 3), whereas the Cu/ZnO catalyst, was more active in the presence of CO_2, as also reported for the Cu/ZnO-Al_2O_3 catalyst system.[13] However, when promoting the Cu/MgO catalyst with only 5 % ZnO (Cu/MgO:Zn, CMZ) the activity in the presence of CO_2 increased significantly, which is in line with earlier reports[13] and indicates the presence of similar surface sites in CZ and CMZ. Interestingly, the catalyst CMZ is active in both CO- and CO/CO_2-hydrogenation, which we assign to the overall high surface area and specifically to some copper surface sites that are not promoted by the chosen low amount of Zn and thus similar to the sites present in CM.

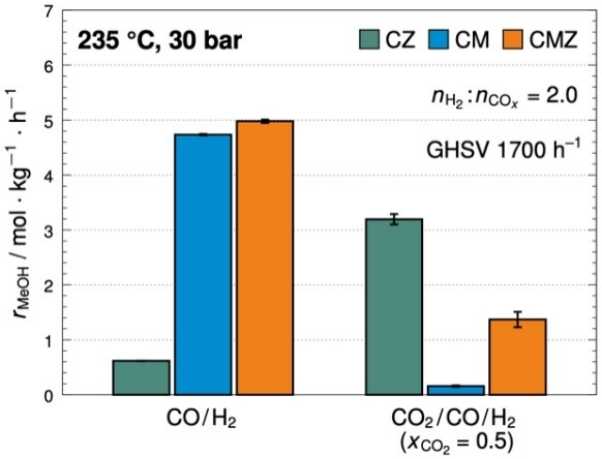

Figure 3. Rate of methanol synthesis from CO/H_2 and CO_2/CO/H_2 with the CZ, CM, and CMZ catalysts reduced at 275 °C and tested at 30 bar, 235 °C, GHSV of 1700 h^{-1} and H_2:CO_x ratio of 2:1.

2.3. Probing the interaction of ZnO with copper particles by *in situ* XRD and XAS

As the CMZ catalyst only contains 5% ZnO, particularly in connection with copper, the structural changes of zinc associated with copper can be much easier followed than in pure Cu/ZnO[11c] or Cu/ZnO/Al_2O_3 catalysts,[10,16] where zinc is in excess and thus a high fraction of spectator species are present. Hence, the CMZ catalyst is ideal to elucidate the structural changes of both copper and zinc, the interaction of $Zn(O)_x$ with Cu and the alloying of the Zn-promoter with copper particles in reducing atmospheres, while the MgO was used to disperse the entire Cu–Zn ensemble, but not contribute to any of these interactions.

As described above, the EDX-TEM image after reduction at 250 °C (Figure 1(b)) shows a clear segregation of Cu and the MgO phase. ZnO stayed well distributed and, thus, can be assumed to remain in close contact with both catalyst components MgO and Cu. Whereas transmission electron microscopy and X-ray photoelectron spectroscopy gave insight into the overall elemental distribution in the catalyst, structural information on crystalline domains and atomic-scale interactions was not obtained using these techniques, in particular also not while their reduction. Hence, both *in situ* X-ray diffraction (XRD) and *in situ* X-ray absorption spectroscopy (XAS) at the Cu K- and Zn K-edge were conducted to obtain this information.

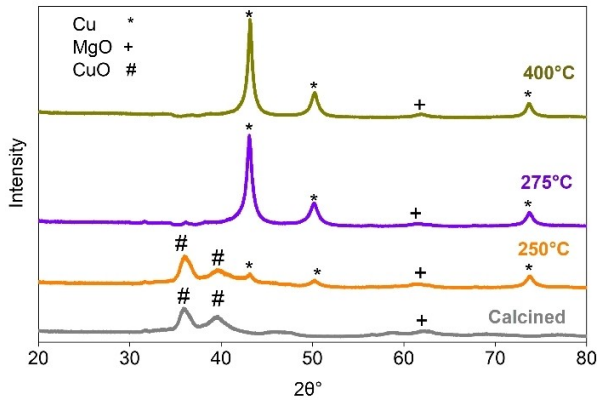

Figure 4. XRD patterns (λ = 1.54 Å) of the CMZ calcined catalyst and the activated catalyst after reduction at 250 °C, 275 °C and 400 °C. Rietveld and Pawley refinement fits are shown in Figure S2.

Selected X-ray diffraction patterns during *in situ* XRD are shown in Figure 4. In the calcined catalyst, typical reflections of CuO with minor contribution of ZnO were observed.[13] At 250 °C, the typical reflections of *fcc*-Cu (lattice spacings (111), (200), and (220) at $2\theta = 43.6°$, 50.8° and 74.7°, respectively) emerge. The observed increase of their intensities at elevated temperature is caused by the further crystallization of metallic copper particles. The broad reflection at $2\theta = 62.3°$ shows the presence of poorly crystalline MgO, while its other reflections (at $2\theta = 36.9°$, 42.8°and 74.6°) could overlap with those of metallic Cu. The diffraction patterns collected at 250 °C show the presence of both Cu and CuO, revealing that during heating in H_2 atmosphere CuO is only partially reduced at 250 °C. A temperature of 250 °C may not be sufficient to fully reduce CuO, especially that in contact with MgO, with 3% H_2/N_2 used in this experiment, which is in agreement with the TPR curves obtained in diluted hydrogen (Figure S4). This is most likely caused by the low hydrogen conditions (imposed by technical and safety regulations) during this reduction treatment compared to typical operating conditions of pure or 50% H_2 in N_2, where a complete reduction of CuO would be achieved. Another reason could be, that because the samples were pressed into pellets for the XRD measurements, internal mass transport or the contact of the powder with the reaction gas was limited.

The average crystallite size of Cu, deduced by Rietveld refinement, was found to be 8.6 nm at 275 °C and 9.8 nm at 400 °C (Table 2), respectively, indicating a low propensity to sintering of the MgO-supported Cu despite the high reduction temperature. While Cu and MgO crystallite sizes increased with temperature, the ZnO particle size slightly decreased when increasing the reducing temperature from 275 °C to 400 °C. Using Rietveld refinement, a ZnO phase was detected during *in situ* XRD, before and after reduction at 275 °C with only little changes between calcined and reduced states (Figure S2), which is assigned to the segregated fraction of ZnO observed in the EDX mapping. This phase was quantified to 1 ± 2% by Rietveld refinement allowing to estimate that approximately half of the Zn species present in the sample were highly dispersed. At 400 °C, the weak reflections at 31.3° of this ZnO

Table 2. Table showing crystallite sizes of the metal components in the catalyst system estimated from XRD.

Phase	Quantity	Calcined	Reduced 275 °C	Reduced 400 °C
CuO	Content [wt.%]	Majority[c]	Not detected	Not detected
		(00l): 4.8 ± 1.0		
	Domain size[a] [nm]	(h00): 2.5 ± 1.0		
	anisotropic needle-like [mm]	(hkl): 2.5 ± 1.0		
Cu	Content [wt.%]	Not detected	68 ± 2	66 ± 2
	Domain size* [nm]		8.6 ± 1.0	9.8 ± 1.0
	A[b] [%]		1.432	1.676
ZnO	Content [wt.])	Minority[c]	Minority[c]	Minority[c]
	Domain size* [nm]	8.9 ± 1	11.7 ± 1.0	8.0 ± 1.0
MgO	Content [wt.%]	Not detected	31 ± 2	31 ± 2
	Domain size* [nm]		3.1 ± 1.0	4.4 ± 1.0

[a] Volume-weighted domain size, [b] Stacking fault probability, [c] Majority/minority phases identified but not quantified.

phase were further diminished, which was accompanied by an increase in the Cu lattice parameter (Table S3) and corresponded to a ZnO particle size decrease (Table 2). The lattice constants determined at the same temperature as the reduction generally depend on temperature and crystallite size (Figure S3) and can therefore not be assigned unambiguously to the formation of Cu–Zn brass.

The XANES spectra of calcined CMZ at the Cu K-edge resembled that of the CuO reference, Figure 5(a). In the Fourier-transform of the EXAFS spectra (Figure 5(b)) calcined CMZ shows a backscattering peak at $R = 1.5$ Å (not corrected for phase shift) which is typical for a Cu–O shell with a further prominent contribution at $R = 2.7$ Å, which indicates the formation of a Cu–Cu shell. Upon reduction at 250 °C, a shoulder at 8980 eV evolved and the white line decreased due to formation of metallic Cu particles. Similarly, these changes are also reflected in the Fourier transform of the in situ recorded EXAFS spectra, where the Cu–Cu scattering path (2.53 Å, CN = 7.6 ± 1.2) (Figure 5(b), Table 3) appeared at 250 °C, indicating the presence of Cu^0. These changes became more pronounced with an increase of the reduction temperature to 275 °C (CN = 8.2 ± 1.6) and 400 °C (CN = 7.6 ± 1.2). As metallic Cu and a Cu–Zn alloy have the same *fcc*-crystal structure and the backscattering of the two neighbors in the periodic table are similar the two metals are indistinguishable by EXAFS and the Cu–Zn alloy formation is only directly visible through the corresponding lattice parameter which was slightly enlarged by Zn incorporation.[17] Since EXAFS was measured at room temperature, any bond distance increase would be assigned to alloying, not thermal effects.

The structural changes and reduction of the ZnO promoter were analyzed by Zn K-edge XANES and EXAFS, Figures 5(c, d). In the XANES region, Figure 5(c) and 6(a), the shoulder at 9659 eV and the scattering feature at 9700 eV characteristic of metallic Zn increased, while the white line intensity characteristic of oxidized $Zn(O)_x$ decreased, as reduction temperatures of 250 °C, 275 °C and 400 °C were applied. The spectral changes were tracked by taking difference-XANES spectra between XANES taken at the three temperatures, Figure 6(b). The difference-XANES between 400 °C and each of the two lower temperatures, 275 °C and 250 °C, revealed the characteristic features that can be interpreted as oxidized and more metallic zinc: the shoulder at 9659 eV and the scattering feature at 9700 eV. The difference-XANES between 275 °C and 250 °C also displays these features very weakly, showing that also in this temperature range a small fraction of Zn, presumably at the interface with Cu, proceeded with reduction. The significance of the experimental XANES features has been confirmed by comparing the spectra to theoretically calculated XANES of DFT-optimized models representing the expected ZnO/Cu and

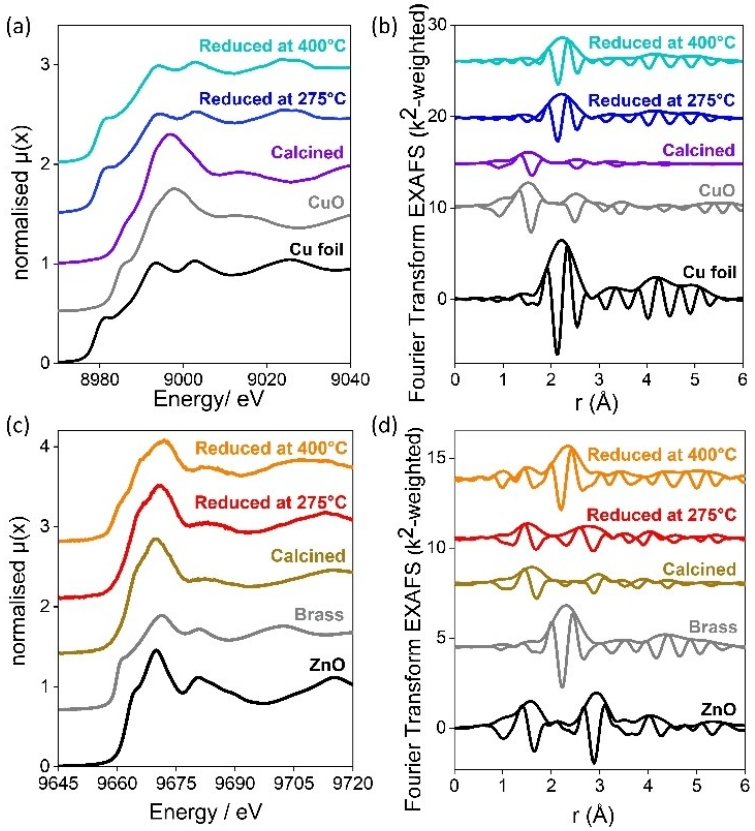

Figure 5. (a) XANES spectra at Cu K-edge, (b) Fourier-transforms EXAFS spectra at the Cu K-edge, (c) XANES spectra at Zn K-edge and (d) Fourier-transforms of EXAFS spectra at Zn K-edge EXAFS of the ZnO-promoted CuO/MgO catalyst (CMZ) and the activated catalyst after reduction at 250 °C, 275 °C and 400 °C. Reference spectra of Cu, CuO, Zn and brass, all measured at room temperature. Corresponding k^2-weighted EXAFS spectra in *k*-space are given as supporting information.

Table 3. Results obtained from EXAFS fitting of calcined catalyst and that after reduction at 250 °C, 275 °C and 400 °C.

Sample	Path	d [Å]	CN	σ^2 [Å^2]	ΔE_0 [eV][a]	R-factor [%][b]
CMZ catalyst, calcined	Zn–O	1.99 ± 0.02	2.8 ± 0.8	0.005 ± 0.004	1.5 ± 2.9	7.0
	Zn–Cu	3.07 ± 0.05	2.4 ± 1.1	0.005 (fixed)		
	Zn–Zn	3.24 ± 0.04	3.7 ± 1.3	0.005 (fixed)		
CMZ catalyst, reduced 250 °C	Cu–Cu	2.53 ± 0.01	7.6 ± 1.2	0.006 ± 0.001	3.5 ± 1.7	3.4
	Zn–O	2.01 ± 0.04	3.8 ± 2.2	0.005 (fixed)	0 (fixed)	29.5
	♦ Zn–Cu	2.55 ± 0.05	5.1 ± 2.8	0.009 (fixed)	0 (fixed)	
	♦ Zn–Zn	2.74 ± 0.04	5.0 ± 2.8	0.009 (fixed)		
CMZ catalyst, reduced 275 °C	Cu–Cu	2.53 ± 0.01	8.2 ± 1.6	0.006 ± 0.000	4.1 ± 0.8	0.8
	Zn–O	2.00 ± 0.04	2.1 ± 0.9	0.005 (fixed)	0 (fixed)	28.8
	♦ Zn–Cu	2.53 ± 0.05	3.5 ± 2.2	0.009 (fixed)	0 (fixed)	
	♦ Zn–Zn	2.72 ± 0.05	5.0 ± 2.8	0.009 (fixed)		
CMZ catalyst, reduced 400 °C	Cu–Cu	2.55 ± 0.01	7.6 ± 1.2	0.007 ± 0.001	7.3 ± 0.6	4.0
	Zn–O	2.04 ± 0.06	1.1 ± 0.6	0.005 (fixed)	5 (fixed)	8.2
	♦ Zn–Cu	2.60 ± 0.02	7.5 ± 1.0	0.009 (fixed)	1.5 ± 0.5	

♦ Paths in metal phase (Cu, brass), [a] Energy correction for edge determination; energies used for background subtraction and models are given in Table S2. Fitting results of the reference compounds Cu, ZnO and brass are given in Table S3, [b] R-factor listed as calculated in Demeter.[18]

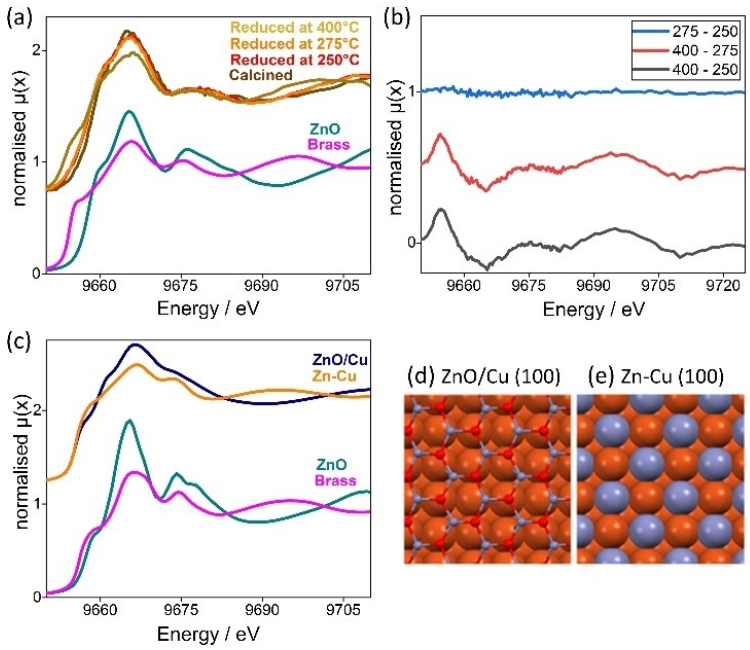

Figure 6. (a) XANES at Zn K-edge, (b) difference spectra of 400 °C–250 °C, 400 °C–275 °C and 275 °C–250 °C (c) calculated spectra of DFT-optimized structural models and references ZnO and brass. Top view of the DFT-optimized structures: (d) oxidized ZnO monolayer on Cu(100) and (e) surface-alloyed Zn–Cu(100), displayed as Cu/ZnO and Cu_3Zn^{SA} in DFT-part, respectively. Color legend: orange, Cu; blue, Zn; red, O. Projected densities of states for each of the calculated XANES spectra are shown in Figure S10.

Zn–Cu states, Figure 6(d, e), as well as the references ZnO and brass. Using the same characteristic spectra features as in the experimental spectra, we found that the calculated Zn K-edge XANES in Figure 6(c) are able to clearly distinguish between oxidized zinc such as a monolayer of ZnO, or other form of dispersed $Zn(O)_x$, on top of metallic Cu postulated at lower reduction temperatures and a surface alloy formed at higher temperatures. Qualitatively, the same differences were observed between the ZnO and brass references. Note that the models represented the extreme states of Zn only, not any mixture of states occurring in reality (oxidized, surface alloy, bulk alloy). Details on the densities of states giving rise to the shoulder and white line are given in Figure S10. The scattering features at 9700 eV and at higher energies likewise show systematic differences for the catalyst and the references, which is further explored in the EXAFS region.

In the Fourier-transform of the EXAFS spectra, Figure 5(d), scattering paths Zn–O (1.99 Å), Zn–Cu (3.07 Å) and Zn–Zn (3.24 Å) were identified in the calcined catalyst by a best EXAFS fit, suggesting a mixed copper-zinc oxide, Table 3. After reduction at 250 °C and 275 °C, scattering identified as Zn–Cu (2.53–2.55 Å) appeared, suggesting a surface alloy between Zn and Cu, as well as Zn–Zn (2.72–2.74 Å) and Zn–O (2.00–2.01 Å) within the $Zn(O)_x$ component, indicating an intermediate state of zinc at the oxide-metal interface as well as fully oxidized zinc atoms. The Zn–Cu and Zn–Zn coordination numbers can be

over-estimated as their scattering partly cancels each other out (Figure S9); the unambiguous interaction between ZnO and Cu is nevertheless supported below by LCF and PCA/MCR-ALS during reduction. After reduction at 400 °C, the Zn–Cu (2.60 Å) scattering became dominant, witnessing Cu–Zn alloying, while some Zn–O (2.04 Å) scattering indicated that some of the zinc oxide – most probably the domains not in contact with copper – remained oxidized, a finding also supported by XRD and TEM. Finally, we probed the XANES of CMZ both at the Cu K-edge and the Zn K-edge during a temperature programmed reduction in 50% H_2/Ar. The results are shown in Figures 7 and 8, respectively.

The appearance of a shoulder at 8979 eV and the decrease in white line during TPR of CMZ at the Cu K-edge already started at about 135 °C (Figure 7(a)). Further analysis by linear combination fitting of the spectra indicated that the reduction of Cu(II) began at around 135 °C. By 200 °C it was completely reduced to metallic Cu (Figure 7(b)). Similarly, the changes

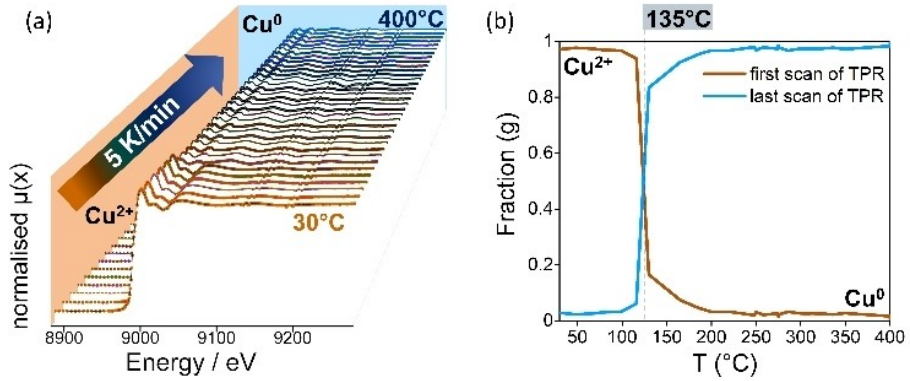

Figure 7. (a) XANES spectra at the Cu K-edge during temperature-programmed reduction (TPR) in 50% H_2/Ar from 30 °C to 400 °C and (b) linear combination fitting (LCF) using the first and the last XANES spectrum as representative for Cu(II) and Cu(0), respectively, as references.

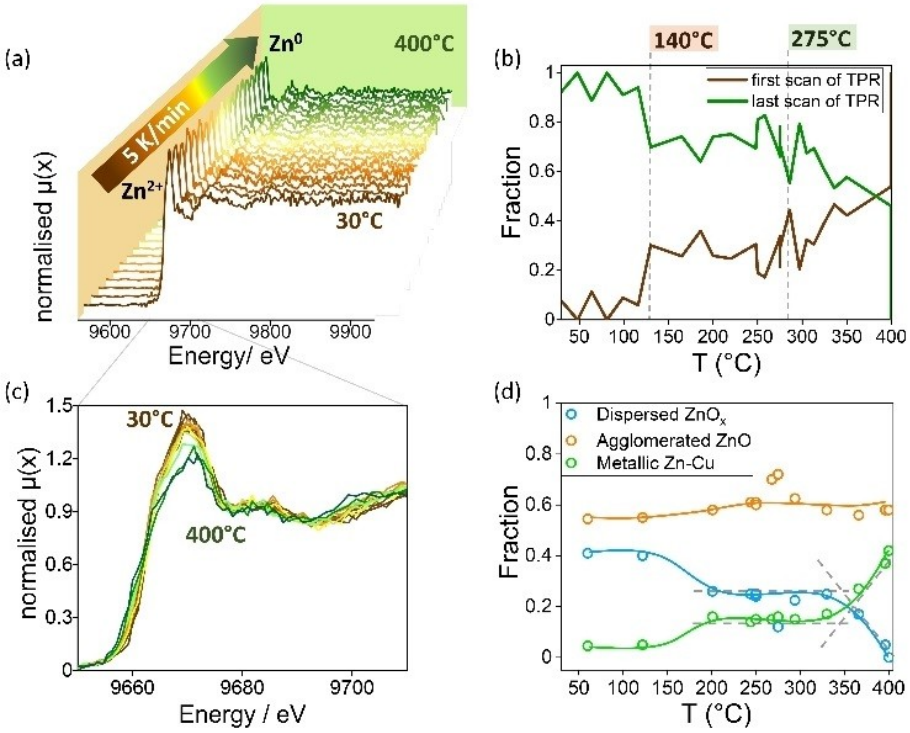

Figure 8. (a) XANES of Zn K-edge during temperature-programmed reduction (TPR) in 50% H_2/Ar from 30 °C to 400 °C, (b) linear combination fitting (LCF) using first and last scans of TPR as references, the two pronounced phase transitions at 140 °C and 275 °C are indicated by vertical dashed lines. (c) XANES of Zn K-edge spectra merged in groups of 2–3 spectra in (a). (d) Concentration profiles of three different Zn-components during TPR, determined by MCR-ALS (lines are as guide for the eye). The number of components was found by principal component analysis (PCA) shown in S11.

during the reduction of CMZ catalyst at the Zn K-edge have been analyzed as a function of temperature during TPR in 50% H_2/Ar (Figure 8). As the XANES spectra show, the white line decreased while the shoulder increased with an increase in the reduction temperature. Two temperatures stand out, 140 °C and 340 °C, where significant changes were observed. At 140–180 °C, almost at the same temperature as for copper reduction, a first change of zinc occurred. No significant changes were detected by XAS in the temperature region from 200 °C to 275 °C. At 340 °C, a further reduction of ZnO was detected in XAS and it further continued up to 400 °C, a temperature typically found in literature (cf. Ref. [12a, 19] At 400 °C Cu–Zn bulk alloy was observed. However, some zinc was still in the oxidized state at 400 °C. As the low ZnO content leads to a formal Zn/Cu ratio of 1:12, we attribute the occurrence of non-reduced ZnO to the fact that it is not in direct contact with copper[20] but located separately on MgO. Hence, we can postulate three co-existing states of zinc during reduction (Figure 8c).

In order to verify this, we conducted principal component analysis (PCA) to determine the number of unique spectral variations and further multicurve resolution alternating linear combination analysis (MCR-ALS) to quantify these variations. The XANES spectra were merged in groups of 2–3 to improve the signal-to-noise ratio, Figure 8(c), and PCA has indeed identified 3 significant components (Figure S11). Further components showed only noise. The principal components (PCs) represented the static average spectrum (PC1), an increase of the low-edge shoulder corresponding to the metallic state (PC2) and a shift of the white line to higher energies corresponding to bulk ZnO (PC3). Note that the components were generated during PCA. The reconstructed XANES spectra by MCR-ALS of the initial dispersed $Zn(O)_x$, metallic Zn and bulk ZnO are shown in Figure S12.and their concentration profile in Figure 8(d). The reduction of $Zn(O)_x$ to the Zn–Cu alloy closely followed the trend observed using LCF, and additionally an almost unchanging bulk ZnO component comprising 55–60% of the Zn species was seen, which peaked between 250–300 °C. At the same temperatures the dispersed $Zn(O)_x$ exhibited a negative peak. We assigned the unchanging portion to ZnO associated with MgO, and the peak (and negative peak in $Zn(O)_x$) to Zn-species associated with Cu that first agglomerated at these temperatures, and afterwards redispersed and alloyed.

Overall, we found using both LCF and MCR-ALS that the formation of reduced surface states started similar as copper at 140 °C and its stable co-existence with dispersed $Zn(O)_x$ between 200 °C and 340 °C corresponds to the catalytically relevant temperature regime for methanol synthesis.

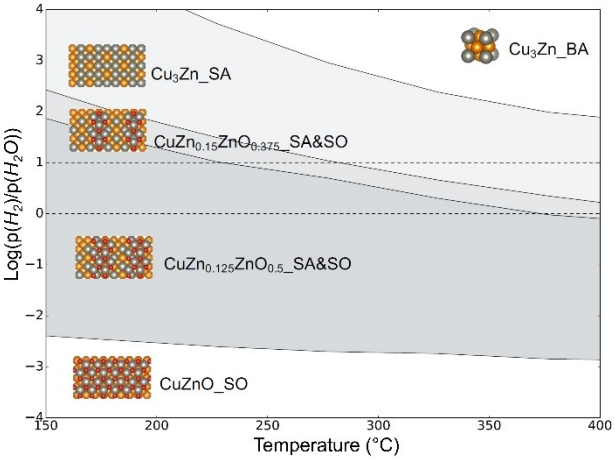

Figure 9. Calculated phase diagram of the ZnO/Cu(100) system as a function of the H_2/H_2O ratio and temperature. All phases are referenced to a Cu(100) surface with 1 ML of ZnO(100) (see also Table S4 for the energies).

2.4. Reduction behavior of Cu/ZnO calculated with DFT

The spectroscopic studies in section 2.3 show that ZnO is reduced slightly at 275 °C and more strongly at 400 °C. Not all ZnO is reduced, probably because some ZnO is distributed on MgO and not in direct contact with Cu. In addition, it has been speculated that first a surface CuZn-alloy forms and higher temperatures result in bulk CuZn-alloy formation.[11c] To further substantiate the effect of the proximity of the Cu surface on the ZnO reducibility, models of single, double and triple ZnO(100) layers over the Cu(100) surface, as well as model of "pure" ZnO (100) and model of the so-called "graphitic" ZnO over Cu(111) were studied. As an estimate of the reducibility of ZnO, we calculated the reduction of ZnO by removal of one oxygen atom from the ZnO layer, creating an oxygen vacancy with a stoichiometry of 1/8 (see Table 4; Figure 9).

Interestingly, reduction of ZnO is more favorable for ZnO that is in contact with the copper surfaces. Moreover, reduction of ZnO is slightly easier for the ZnO(100) facet compared to ZnO in the graphitic form. Thicker ZnO layers (as represented by two or three ZnO(100) layers over Cu(100), on the other hand, are more difficult to reduce. These calculations thus indicate that the dispersion of ZnO over the copper surface greatly influences its reducibility. The reduction of ZnO and corresponding formation of the surface alloy (denoted SA) was calculated according to Equation (1):

$$Cu_x(ZnO)_y + iH_2 \rightarrow Cu_{x-i}Zn_i(ZnO)_{y-i} + iH_2O + iCu^{bulk} \quad (1)$$

Table 4. Oxygen vacancy formation energy for graphitic ZnO single layer over Cu(111), ZnO(100) (single, double and triple layer) over Cu(100) and ZnO (100)-slab. All energies are given relative to the ZnO(100) slab.

	$ZnO_{graphitic}$/Cu(111)	$(ZnO)_1$/Cu(100)	$(ZnO)_2$/Cu(100)	$(ZnO)_3$/Cu(100)	ZnO(100)
Oxygen vacancy [eV]	−0.27	−0.37	0.22	0.20	0

We calculated the phase diagram of the ZnO_x/Cu system (see Figure 9). The ZnO/Cu in its (100) form (see Table 4) is used as a reference, see Figure S13 for all structures. We calculated how the ZnO layer gets partially reduced and alloyed into the Cu(100) surface. At high H_2/H_2O ratios and higher temperatures the system gets reduced to the CuZn bulk alloy (brass). Importantly, there is a large range where the calculations predict the formation of CuZn surface alloys, with the amount of Zn in the Cu surface increasing with increasing temperature. The reason that the surface alloy forms at considerably weaker reducing conditions is because its stability is larger than that of the bulk alloy, which also means that the heat of formation of CuZn surface alloys is larger than that of the bulk alloy.

This is also evident from Table 5, where the Zn alloying energy of various surface terminations of copper is compared to that of the bulk. The formation of the bulk alloy (Cu:Zn ratio of 3:1) is calculated to −0.27 eV. All CuZn surface alloys considered here are more stable by about 0.15 to 0.25 eV, in agreement with earlier segregation studies on the Zn/brass system.[20] Likewise, our calculations reveal that Zn stays in the surface, as sub-surface Zn is calculated to be less stable by 0.16 eV and 0.23 eV for the Cu(111) and Cu(100) surface, respectively. The heat of formation is getting larger for Zn substitution at more undercoordinated sites, indicating that edges and corners are substituted by Zn before substitution at the close-packed (111) facet occurs, in agreement with earlier theoretical studies.[21] These theoretical calculations, thus, nicely confirm the experimental findings. Moreover, they offer a rationale for why the formation of Cu–Zn surface alloys occurs at lower temperature than that of brass. Note that the undercoordinated sites are calculated to be alloyed with Zn atoms with the highest heat of formation. This is especially interesting as these sites have been postulated to be responsible for the high CO_2 hydrogenation activity of the industrial $Cu/ZnO/Al_2O_3$ catalyst.[4b]

2.5. Discussion on the structural changes occurring during reduction

In various studies, the role of zinc in $Cu/ZnO/Al_2O_3$ catalysts has been discussed ranging from oxidic ZnO species to surface alloys and brass formation. For example, Frei et al.[16] have reported the reduction of ZnO and Grunwaldt et al.[11c] have shown the effect of alloying of Zn into the copper particles. However, in all these cases an excess of zinc was present. In the present study a Cu/MgO model catalyst has been used that is promoted with ~5% ZnO. This allowed us to monitor the structural changes occurring on the catalyst with a higher specificity regarding the state of Zn. The catalytic studies show, in agreement with an earlier study by Behrens et al.,[13] that ZnO is able to promote the CO_2 hydrogenation on this catalyst, which was substantially less active on CM without ZnO addition, and in our *in situ* experiment even inactive. Hence, this CMZ catalyst can be regarded as an inverse catalyst containing the relevant $Zn(O)_x$ species on the Cu surface and it is thus able to mimic the reactions occurring in the technical catalyst. The structural evolution probed by *in situ* techniques and in agreement with the calculated phase diagram (Figure 9) unravels that the copper constituent is first reduced in H_2. This is followed by reduction of ZnO only at slightly higher temperatures. Our analysis reveals that, ZnO that is in close contact with copper is reduced more easily due to the high stability of the formed surface alloy. Importantly, the surface alloy is more stable than the bulk alloy, which is only formed at higher temperatures. This reduction sequence is depicted schematically in Figure 10.

While other groups have also designed model systems, e.g. on alumina and silica[17] or 5%Cu/ZnO[11b,c] the advantage of the present system is that magnesium oxide is fulfilling the stabilizing role of ZnO while acting as an inert support. Further, Cu particles are rather small and there is no binary phase between Cu and MgO which allows to specifically probe the interaction of ZnO with copper. According to MCR-ALS (Fig-

Table 5. Energy of alloying for a single Zn atom in Cu bulk and different Cu-facets calculated by DFT referenced to metallic Zn in the bulk. Zn substitutions are 0.17 ML for Cu(111), Cu(100), Cu(211), Cu(221) and 0.25 ML for Cu(110).

Structure	Cu bulk	Cu(111)	Cu(100)	Cu(110)	Cu(211)	Cu(221)	Cu(532)
Alloying energy [eV]	−0.27	−0.43	−0.50	−0.55	−0.51	−0.48	−0.52

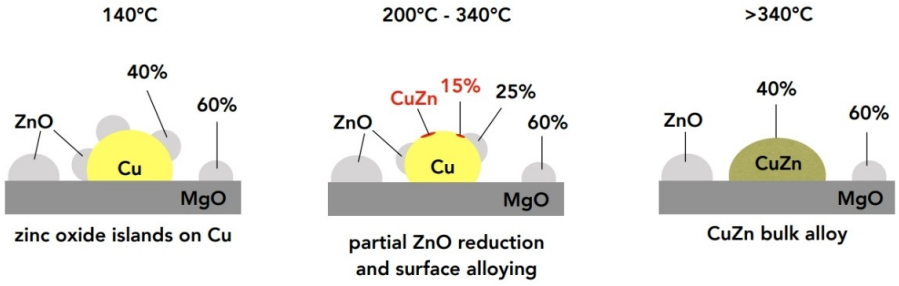

Figure 10. Schematic illustration of the changes occurring in the catalyst during reduction with reduction of copper at 140 °C, start of surface alloying at 180 °C, and finally bulk alloy formation above 340 °C. Some ZnO that is not in contact with Cu particles remains unreduced.

ure 8), 15–20% of Zn are in direct contact with copper and thus 0.7–1.0% of the 5% ZnO on the Cu-catalyst are reduced. Considering about 10% dispersion of copper (based on 10 nm large particles) the surface Zn:Cu-ratio is about 1:5. Such a reduction of zinc with bulk methods like in situ XAS is hardly visible for a conventional catalysts where typically 20% ZnO are present together with 70% copper, which would mean that instead of the observed 15–20% reduction at the interface (Figure 8(d)) only 3.5–5.0% would be reduced at the interface which would be hardly detectable by *in situ* X-ray absorption spectroscopy.

3. Conclusion

We designed an inverse Cu/MgO:ZnO as model catalyst to probe the interaction between Cu and ZnO during different reduction temperatures, particularly focusing on the state of Zn. The synthesis conditions allowed us to incorporate controlled amounts of Zn into the precursor – mcguinnessite, so as to specifically analyze the catalytic promotor effects of ZnO. During reduction, a favorable nanostructure with uniformly dispersed Cu particles in good contact with dispersed ZnO phase was obtained. The particle size slightly increased upon reduction at higher temperatures for Cu and MgO. However, a slight decline in the particle size of ZnO was observed upon increasing the reduction temperature.

The reduction behavior of Cu/MgO:ZnO calcined catalyst analyzed by *in situ* XRD and XAS allowed to assess the structural changes of both copper as well as those of ZnO, which are often obscured by the high fraction of spectator species on other model catalysts. Temperature-programmed reduction at 275 °C (mild reduction) and 400 °C (harsh reduction) brought the catalyst to two interesting states: these are the Zn–Cu surface alloy (200–275 °C) and the Zn–Cu bulk alloy (400 °C). This was both supported by experimental and theoretical studies. Note that the issue of active site motifs is still controversially discussed in the literature.[12a,17,22,23] While the preparation of our inverse catalyst allows for the identification of the formation of a CuZn surface alloy, correlating any surface structure with methanol syntheses activity warrants *operando* studies. We believe that employing this inverse catalyst with a strongly decreased ZnO content operando studies might be able to close these ongoing controversies. The study shows that the fraction of surface alloy is small and only special model catalysts allow maximizing the species of Zn at the interface. Complete reduction of ZnO was observed at 400 °C for the fraction of ZnO that was in direct contact with metallic copper. Density functional theory calculations allowed exploring the feasibility of ZnO reduction in the presence of Cu at different reductive conditions and temperatures, confirming that the reason for the formation of the Cu–Zn surface alloy at lower temperatures is connected to its higher stability compared to the bulk alloy. The catalyst was active and selective for CO_2 hydrogenation and acts as good model catalyst to study Cu/Zn interaction. Probing the Cu/Zn interaction during reduction support studies that report that reduced Zn-species at the interface play an important role in methanol synthesis.

Our study highlights the necessity to rationally design good model catalysts that allow the unobstructed observation of the catalytically active surface and its changes *via in situ* methods, while avoiding spectroscopic background from non-active bystander compounds. This is in particular important if one wants to follow the onset and formation of surface alloying. Here, we have shown that a combination of XANES, EXAFS and MCR-ALS as well as DFT calculations is needed to elucidate CuZn surface alloy formation and that this has only been possible because of the use of an inverse ZnO/Cu/MgO catalyst, strongly decreasing the amount of spectator ZnO species. To directly link the observed surface alloy formation with methanol synthesis activity, an in-depth identification of structure-activity relationships can be obtained by more elaborate *operando* studies.

Experimental section

Catalyst Preparation: The CMZ catalyst was prepared according to a synthesis procedure described in detail elsewhere.[13] In brief, 75 g of the mixture of the nitrate solutions of 1.0 M of Cu/Mg (70:30) were co-precipitated at 65 °C to synthesize hydroxycarbonates. A solution of 1.6 M Na_2CO_3 was used as a precipitating agent in an automated lab reactor (OptiMax, Mettler Toledo) at constant pH = 9.0. The precipitates were aged for 120 min in the mother liquor, filtered, washed and dried to yield the amorphous mcguinnessite precursor, impregnated with 4.0 mL of 0.27 M zinc nitrate solution. The mixture was subsequently calcined in static air for 3 h at 350 °C (2 K/min). A binary Cu/ZnO reference catalyst CZ was prepared accordingly (following the general recipe of the academic reference Cu/ZnO:Al, but without addition of Al),[24] using 75 g of a 1.0 M Cu/Zn nitrate solution (70:30) for co-precipitation at 65 °C and pH 6.5. Again, the precipitate was aged for 120 min in the mother liquor, filtered, washed and dried to yield poorly crystalline zincian malachite in this case. Calcination was carried out in static air for 3 h at 350 °C (2 K/min).

Tests of the catalytic activity: Catalytic tests for the comparison of the CM, CMZ and CZ catalysts were performed in a stainless steel fixed-bed reactor (inner diameter 2.6 mm, at Avantium Technologies) with 150 mg of the Zn-impregnated Cu/MgO calcined catalyst (sieve fraction 125–250 μm) packed in a pre- and post-bed of about 200 mg SiO_2. The catalyst was activated by reduction under 5% H_2/N_2 at 275 °C (heating rate 5 K/min, dwell time 4 h) and ambient pressure. The gas feed was adjusted to a H_2/CO_x ratio of 2.0 and a GHSV of 1700 h^{-1}. After allowing the catalysts to stabilize for ca. 200 h, measurements were done at 30 bar and various temperatures, here reported at a temperature of 235 °C. Gas lines between reactor and exhaust were heated to prevent condensation of methanol and water. The products were analyzed at the depressurized outlet at ambient pressure using a gas chromatograph.

Characterization: The Cu:Mg:Zn ratio of the catalyst was determined by atomic absorption spectroscopy (AAS), performed on a Themo Fisher iCE-3500 AAS after dissolving the samples in nitric acid overnight. CHNS analysis was carried out by combustion of the sample together with V_2O_5 in a EuroVector EA3000.

The N_2 adsorption-desorption profiles were measured at a Nova 3200e sorption station from Quantachrome. Purified and water-free nitrogen was used. The partial pressures referred to reference cell were recorder between $p/p_0 = 0.0$ and 0.9 at 77 K to create the complete isotherm profile. The surface areas of precursors and

calcined samples were calculated by applying the Brunauer-Emmett-Teller (BET) equation to the N_2 adsorption data in the range of $p/p_0 = 0.07$ to 0.40 of the pressure ratio. The sample was first degassed under vacuum at 80 °C to remove any adsorbed impurity gases.

Temperature-programmed reduction (TPR) profile was obtained by heating the sample to 250 °C in 10 % H_2/Ar at a heating rate of 6 K/min. Hydrogen consumption was determined by analysis of the eluted gas using a thermal conductivity detector at the outlet.

Transmission electron microscopy (TEM) images were obtained on a JEOL 2200FS microscope. The voltage of electron acceleration was 200 kV. Elemental mapping with energy-dispersive X-ray spectroscopy (EDX) was used to determine the elemental composition and distribution in the sample. The images were processed using AZtec software. Both calcined and reduced samples were analyzed. The reduced sample was prepared in a glove box and placed on an air-free transfer holder. The samples were dispersed with ethanol onto nickel TEM grids with lacey carbon film.

N_2O-reactive frontal chromatography (N_2O-RFC) was conducted in a quartz glass U-tube reactor with an inner diameter of about 4 mm. 100 mg of a 250–355 micrometer sieve fraction of the catalyst was used. Before recording the N_2O consumption the sample was reduced in a gas containing 2.1 % H_2 in He. To ensure complete adsorbate free surface the reduced sample was treated for 1 h at 220 °C in a He stream followed by cooling to room temperature. The N_2O decomposition experiment was performed with 1 % N_2O in He at room temperature and atmospheric pressure with a volume flow of 10 ml/min. The consumption of N_2O molecules was determined by a calibrated quadrupole mass spectrometer (Balzer GAM 400). Calculating the metal surface areas and other quantities related to N_2O-RFC are performed according to DIN 66136-1.

X-ray photoelectron spectroscopy: X-ray photoelectron spectroscopy (XPS) was recorded by using a ULVAC-Phi Versaprobe II TM spectrometer using a monochromatized Al-Kα beam with a beam size of 100 μm and a spectral resolution of 0.5 eV. A dual beam charge compensation of electrons and slow-moving Argon ions was used to reduce charging effects. The samples were reduced *ex situ* (10 % H_2/Ar, 5 K/min, 250 °C, 1 h) and transported in inert gas atmosphere to the XPS machine without exposure to air. All spectra were referenced to the position of the carbon peak at 284.8 eV binding energy. The detected peaks were fitted using the software CasaXPS. All non-metallic peaks were fitted using a Gaussian-Lorentzian product function and a Shirley background. For elemental Cu an asymmetric peak shape was used.

***In situ* X-ray diffraction**: X-ray diffraction (XRD) patterns were recorded *in situ* on a Stoe Stadi P diffractometer, equipped with a Cu anode and a Ge(111) monochromator (Cu K_α radiation, $\lambda = 1.54059$ Å). The diffraction patterns were recorded in reflection mode, with static source and the sample cup and detector in $\theta/2\theta$-geometry. The sample was pressed into a pellet and placed in the sample cup, without rotating the pellets. The patterns of calcined and reduced catalysts were recorded in the 2θ-range between 20° and 80° with a step size of 0.015° and total measurement time of 60 min. The catalysts were reduced in 3 % H_2/He (100 mL/min total flow) at 275 °C and 400 °C using a heating rate of 10 K/min in an Anton Paar HTK 1200N furnace. During the measurement the temperature was kept constant. Structural and microstructural analysis via Rietveld refinement[25] was performed using the software TOPAS Academic version 6.[26] The background contribution caused by the oven chamber was determined by measuring the empty setup. For Rietveld refinement this background was scaled accordingly. The instrumental contribution to the peak broadening was determined by measuring a NIST line shape and peak position standard material (Si SRM 640d). The accuracy of the crystallite size determination given as the volume weighted domain size was tested by analyzing a NIST nanoparticle standard (ZnO SRM 1979 A).[27] The standard was measured using the same setup and the accuracy was determined to be ±1 nm. A stacking fault probability α was calculated using Equation (2) by Warren based on single peak fit of Cu(111) and Cu(200) reflections.[28]

$$\Delta(2\theta_{200} - 2\theta_{111})^\circ = \frac{-90\sqrt{3}\alpha}{\pi^2}\left(\frac{\tan\theta_{200}}{2} + \frac{\tan\theta_{111}}{4}\right) \quad (2)$$

The ideal peak positions of reference data of *fcc*-Cu (ICSD 235809) was used to determine $\Delta(2\theta_{200} - 2\theta_{111})$. A detailed description of the procedure can be found elsewhere.[29] The relative intensities of Cu and ZnO phases were corrected by using a preferred orientation correction approach by March and Dollase (see e.g. Ref. [30]). Cu showed a Cu(111) and ZnO a ZnO(001) preferred orientation, respectively. The anisotropic Lorentzian peak broadening was taken into account by using a non-physical model of spherical harmonics in tan2θ-dependence. For the room temperature phase of the calcined catalyst a structureless Pawley fit was applied, based on the unit cells of CuO (Tenorite – ICSD 67850) and ZnO (Wurtzite – ICSD 67848).[31] The CuO peaks are anisotropically broadened, which was taken into account by applying an (*hkl*)-dependent crystallite shape model, revealing a needle-like habitus of the CuO crystallites. Fit quality was assessed by the weighted-profile R-factor, R_{wp}[32] with weights w_i and intensities y_i, defined as [Eq. (3)]:

$$R_{wp} = \left\{\frac{\sum_i w_i[y_i(obs) - y_i(calc)]^2}{\sum_i w_i[y_i(obs)]^2}\right\}^{\frac{1}{2}} \quad (3)$$

***In situ* X-ray absorption spectroscopy (XAS)**: *In situ* XAS measurements were performed at Karlsruhe Institute of Technology (KIT) synchrotron at the CATACT wiggler beamline using a Si(111) double-crystal monochromator. The XAS data were recorded at the Cu K-edge (8979 eV) in transmission mode and at the Zn K-edge (9659 eV) in fluorescence mode using a Vortex fluorescence detector. EXAFS was measured up to $k = 13$ Å^{-1} for both edges. Reference Cu and Zn foils were used for energy calibration. For the *in situ* TPR measurements, a quartz capillary micro-reactor of diameter 1.5 mm was used, containing 8 mg sample prepared by diluting the catalyst 1:5 by mass with SiO_2 and sieving in the fraction 100–200 μm. The sample was packed on both sides with glass wool plugs. A resistive heater was used to heat and maintain the temperature of the capillary. A flow of 50 % H_2/Ar at a total gas flow of 80 mL/min was used. Continuous scanning (5 mins/scan) of the XANES region was performed during reduction experiments and a full EXAFS scan was done after cooling to room temperature. The catalyst mixture was heated to 250 °C, 275 °C and 400 °C to study the extent of Cu–Zn interaction during this activation of the model catalyst. Initially, the catalyst was reduced at 250 °C (5 K/min, hold for 10 mins) and then cooled to room temperature to get a good quality EXAFS scan. The catalyst was re-heated to a temperature of 275 °C (20 K/min up to 250 °C, then 5 K/min up to 275 °C, hold for 30 mins) and cooled to room temperature for EXAFS scans. Next, the catalyst was reduced at 400 °C (20 K/min up to 275 °C, then 5 K/min until 400 °C and hold for 10 mins) before cooling down to measure EXAFS scan.

The raw data was then treated using Athena and Artemis.[18] The energies of the spectra were calibrated and aligned in the derivative mode to reference metal foils to correct any energy shifts, and the spectra were normalized. By linear combination fitting (LCF) the amount of oxidized and reduced Cu fractions

during TPR were calculated, using a merge of five initial spectra at RT and the merge of five final spectra at 400 °C.

For reduced samples, the first Cu–Cu shell in the sample EXAFS spectra was refined. The amplitude reduction factor, $S_0^2 = 0.86 \pm 0.03$, was refined from the first Cu–Cu shell of Cu foil. Zn K-edge EXAFS spectra of the calcined and reduced catalyst were refined using single-scattering paths from Zn-doped CuO and brass. $S_0^2 = 0.88 \pm 0.01$ for Zn K-edge spectra was refined from the first Zn–O path of ZnO. In some fits we fixed the values of σ^2 to the same values that were obtained when fitting was possible (Tables 3 and S3; Zn–O: 0.005 Å^2; Zn–Zn and Zn–Cu: 0.009 Å^2). ΔE_0 was fixed so that final $E_0^{final} = E_0$ (from background subtraction, Table S2) $+ \Delta E_0$ (from fitting, Table 3) resulted to approximately 9664–9665 eV for both oxidic and metallic structures, as obtained for ZnO and brass references (Tables S2 and S3).

Principle component analysis (PCA) of the reduction data was conducted in order to determine the number of principle components needed for reconstructing the XANES data series. The multivariate resolution alternating linear combinations (MCR-ALS) analysis for the reconstruction and quantification of the reference states of Zn was conducted using the MCR-ALS GUI 2.0 in a MATLAB environment.[33] The three references extracted using the MCR-ALS method[34] were used for their quantification by linear combination analysis.

The changes occurring in Zn K-edge XANES spectra before and after reduction were analyzed qualitatively by comparing with theoretically calculated spectra. XANES spectra were calculated of DFT-optimized monolayer-ZnO on Cu(100) and surface Zn–Cu(100) alloy models. Details of the DFT-calculation, see section below. The calculations of XANES and projected densities of states (DOS) were conducted with the FEFF 9.9.1code[35] using Hedin-Lundquist exchange-correlation potentials, self-consistent field calculations within 4.5 Å of each atom and full multiple scattering calculations within 9.5 Å. The random-phase approximation (RPA) core-hole rule was used for the absorber to take core-screening into account. Likewise, the projected densities of states of the Zn absorber atoms and Cu and O neighbors were calculated around the edge position.

Density functional theory calculations: The density functional theory (DFT) calculations were performed using the Vienna Ab Initio Simulation Package (VASP)[36] in connection with the Atomic Simulation Environment (ASE).[37] A plane-wave basis set with a cutoff energy of 450 eV, the projector augmented wave method (PAW)[38] and the Bayesian Error Estimation Functional with van der Waals correlations (BEEF-vdW)[39] exchange correlation functional were used. The infinite slab models used to construct ZnO_x/Cu phase diagram consist of four layers thick 4×2 Cu(100) unit cells in the *xy*-plane, separated by more than 16 Å vacuum in the *z*-direction. During geometry optimizations bottom two layers were kept fixed and upper 2 layers were allowed to relax. Alloy structures were obtained by substituting surface and sub-surface copper atoms by zinc. ZnO over Cu was modelled by superposition of 3×1 large ZnO(110) single layer over 4×2 large Cu(100) unit cell. Lattice mismatch between ZnO and Cu was 2.39% in the *x* and 4.07% in the *y*-direction. The Brillouin zones were sampled using a 2×4×1 Monkhorst-Pack *k*-point grid.[40] The so-called graphitic ZnO was modelled as 3×3 ZnO single layer over four layer thick 4×4 large Cu(111) unit cell (referred to as $ZnO_{graphitic}$/Cu(111)), sampled using 3×3×1 *k*-points. Lattice mismatch for this structure was 4.07% in both *x* and *y*-directions. The convergence criterion for geometry optimization was a maximum force of 0.01 eV/Å. Spin polarization was not considered in the calculations.

Acknowledgements

We acknowledge the CATACT beamline at KIT synchrotron (KARA) for providing beamtime, specifically Dr. Anna Zimina for technical support during XAS measurements. We thank Avantium Technologies, Amsterdam, the Netherlands for conducting catalytic tests. Dr. Steffen Czioska is gratefully acknowledged for conducting MCR-ALS analysis. Support by Dr. Ulrich Hagemann (XPS) and Dr. Markus Heidelmann (TEM) of Interdisciplinary Center for Analytics on the Nanoscale (ICAN) of the University of Duisburg-Essen (DFG RIsources reference: RI 00313), a DFG-funded core facility (Project Nos. 233512597 and 324659309), is gratefully acknowledged.We thank Philipp Schwiderowski and Martin Muhler for providing the N_2O chemisorption capacities. We gratefully acknowledge the DFG SPP 2080 programme for funding during this project (BE 4767/3-1, GR 3987/18-1, STU 703/3-1). The authors gratefully acknowledge support from the state of Baden-Württemberg through bwHPC (bwUniCluster and JUSTUS, RV bw17D01), and by the Helmholtz Association. MB and BM gratefully acknowledge the financial support from the Mercator Research Center Ruhr (MERCUR, Pe-2018-0034). Open Access funding enabled and organized by Projekt DEAL.

Conflict of Interest

The authors declare no conflict of interest.

Keywords: Copper catalyst · methanol synthesis · ZnO promoter · *in situ* X-ray absorption spectroscopy · *in situ* X-ray diffraction · copper zinc alloy · density functional theory · strong metal-support interaction

[1] a) F. Schüth, *Chem. Ing. Tech.* **2011**, *83*, 1984–1993; b) G. A. Olah, *Angew. Chem. Int. Ed.* **2005**, *44*, 2636–2639; *Angew. Chem.* **2005**, *117*, 2692–2696.
[2] K. F. Kalz, R. Kraehnert, M. Dvoyashkin, R. Dittmeyer, R. Gläser, U. Krewer, K. Reuter, J.-D. Grunwaldt, *ChemCatChem* **2017**, *9*, 17–29.
[3] a) M. Behrens, *Angew. Chem. Int. Ed.* **2016**, *55*, 14906–14908; *Angew. Chem.* **2016**, *128*, 15128–15130; b) D. Sheldon, *Johns. Matthey Technol. Rev.* **2017**, *61*, 172–182.
[4] a) R. van den Berg, G. Prieto, G. Korpershoek, L. I. van der Wal, A. J. van Bunningen, S. Lægsgaard-Jørgensen, P. E. de Jongh, K. P. de Jong, *Nat. Commun.* **2016**, *7*, 13057 (1–7); b) M. Behrens, F. Studt, I. Kasatkin, S. Kühl, M. Hävecker, F. Abild-Pedersen, S. Zander, F. Girgsdies, P. Kurr, B.-L. Kniep, *Science* **2012**, 336, 893–897.
[5] a) S. Kuld, C. Conradsen, P. G. Moses, I. Chorkendorff, J. Sehested, *Angew. Chem. Int. Ed.* **2014**, *53*, 5941–5945; *Angew. Chem.* **2014**, *126*, 6051–6055; b) F. Liao, Y. Huang, J. Ge, W. Zheng, K. Tedsree, P. Collier, X. Hong, S. C. Tsang, *Angew. Chem. Int. Ed.* **2011**, *50*, 2162–2165; *Angew. Chem.* **2011**, *123*, 2210–2213; c) T. Lunkenbein, J. Schumann, M. Behrens, R. Schlögl, M. G. Willinger, *Angew. Chem.* **2015**, *127*, 4627–4631; *Angew. Chem. Int. Ed.* **2015**, *54*, 4544–4548.
[6] T. Fujitani, J. Nakamura, *Catal. Lett.* **1998**, *56*, 119–124.
[7] J. T. Sun, I. S. Metcalfe, M. Sahibzada, *Ind. Eng. Chem. Res.* **1999**, *38*, 3868–3872.
[8] F. Studt, M. Behrens, E. L. Kunkes, N. Thomas, S. Zander, A. Tarasov, J. Schumann, E. Frei, J. B. Varley, F. Abild-Pedersen, *ChemCatChem* **2015**, *7*, 1105–1111.
[9] V. Schott, H. Oberhofer, A. Birkner, M. Xu, Y. Wang, M. Muhler, K. Reuter, C. Wöll, *Angew. Chem. Int. Ed.* **2013**, *52*, 11925–11929; *Angew. Chem.* **2013**, *125*, 12143–12147.

[10] M. Zabilskiy, V. L. Sushkevich, D. Palagin, M. A. Newton, F. Krumeich, J. A. van Bokhoven, *Nat. Commun.* **2020**, *11*, 2409 (1–8).
[11] a) J. Schumann, M. Behrens, R. Schlögl, R. Schomäcker, *ACS Catal.* **2015**, *5*, 3260–3270; b) B. S. Clausen, J. Schiøtz, L. Gråbæk, C. V. Ovesen, K. W. Jacobsen, J. K. Nørskov, H. Topsøe, *Top. Catal.* **1994**, *1*, 367–376; c) J.-D. Grunwaldt, A. M. Molenbroek, N. Y. Topsøe, H. Topsøe, B. S. Clausen, *J. Catal.* **2000**, *194*, 452–460; d) J. Frost, *Nature* **1988**, *334*, 577; e) W. Jansen, J. Beckers, J. van der Heuvel, A. D. van der Gon, A. Bliek, H. Brongersma, *J. Catal.* **2002**, *210*, 229–236.
[12] a) N. J. Divins, D. Kordus, J. Timoshenko, I. Sinev, I. Zegkinoglou, A. Bergmann, S. W. Chee, S. Widrinna, O. Karslıoğlu, H. Mistry, M. Lopez Luna, J. Q. Zhong, A. S. Hoffman, A. Boubnov, J. A. Boscoboinik, M. Heggen, R. E. Dunin-Borkowski, S. R. Bare, B. Roldan Cuenya, *Nat. Commun.* **2021**, *12*, 1435; b) J. Nakamura, Y. Choi, T. Fujitani, *Top. Catal.* **2003**, *22*, 277–285.
[13] S. Zander, E. L. Kunkes, M. E. Schuster, J. Schumann, G. Weinberg, D. Teschner, N. Jacobsen, R. Schlögl, M. Behrens, *Angew. Chem. Int. Ed.* **2013**, *52*, 6536–6540; *Angew. Chem.* **2013**, *125*, 6664–6669.
[14] M. B. Fichtl, J. Schumann, I. Kasatkin, N. Jacobsen, M. Behrens, R. Schlögl, M. Muhler, O. Hinrichsen, *Angew. Chem. Int. Ed.* **2014**, *53*, 7043–7047; *Angew. Chem.* **2014**, *126*, 7163–7167.
[15] A. Tarasov, J. Schumann, F. Girgsdies, N. Thomas, M. Behrens, *Thermochim. Acta* **2014**, *591*, 1–9.
[16] E. Frei, A. Gaur, H. Lichtenberg, C. Heine, M. Friedrich, M. Greiner, T. Lunkenbein, J.-D. Grunwaldt, R. Schlögl, *ChemCatChem* **2019**, *11*, 1587–1592.
[17] E. Frei, A. Gaur, H. Lichtenberg, L. Zwiener, M. Scherzer, F. Girgsdies, T. Lunkenbein, R. Schlögl, *ChemCatChem* **2020**, *12*, 4029–4033.
[18] B. Ravel, M. Newville, *J. Synchrotron Radiat.* **2005**, *12*, 537–541.
[19] Y. Okamoto, K. Fukino, T. Imanaka, S. Teranishi, *J. Phys. Chem.* **1983**, *87*, 19, 3747–3754.
[20] a) K.-D. Jung, O.-S. Joo, S.-H. Han, *Catal. Lett.* **2000**, *68*, 49–54; b) M. Spencer, *Surf. Sci.* **1987**, *192*, 323–328; c) M. Spencer, *Surf. Sci.* **1987**, *192*, 336–343.
[21] S. Kuld, M. Thorhauge, H. Falsig, C. F. Elkjær, S. Helveg, I. Chorkendorff, J. Sehested, *Science* **2016**, *352*, 969–974.
[22] K. Chanchlani, R. Hudgins, P. Silveston, *J. Catal.* **1992**, *136*, 59–75.
[23] N. D. Nielsen, A. D. Jensen, J. M. Christensen, *J. Catal.* **2021**, *393*, 324–334.
[24] J. Schumann, T. Lunkenbein, A. Tarasov, N. Thomas, R. Schlögl, M. Behrens, *ChemCatChem* **2014**, *6*, 2889–2897.
[25] H. Rietveld, *J. Appl. Crystallogr.* **1969**, *2*, 65–71.
[26] A. A. Coelho, *J. Appl. Crystallogr.* **2018**, *51*, 210–218.
[27] a) J. P. Cline, M. H. Mendenhall, J. J. Ritter, D. Black, A. Henins, J. E. Bonevich, P. S. Whitfield, J. J. Filliben, *J. Res. Natl. Inst. Stand. Technol.* **2020**, *125*; b) D. Balzar, N. Audebrand, M. Daymond, A. Fitch, A. Hewat, J. Langford, A. Le Bail, D. Louër, O. Masson, C. N. McCowan, *J. Appl. Crystallogr.* **2004**, *37*, 911–924.
[28] B. Warren, *J. Appl. Phys.* **1961**, *32*, 2428–2431.
[29] T. Kandemir, I. Kasatkin, F. Girgsdies, S. Zander, S. Kühl, M. Tovar, R. Schlögl, M. Behrens, *Top. Catal.* **2014**, *57*, 188–206.
[30] W. Dollase, *J. Appl. Crystallogr.* **1986**, *19*, 267–272.
[31] G. Pawley, *J. Appl. Crystallogr.* **1981**, *14*, 357–361.
[32] B. H. Toby, *Powder Diffr.* **2006**, *21*, 67–70.
[33] J. Jaumot, A. de Juan, R. Tauler, *Chemom. Intell. Lab. Syst.* **2015**, *140*, 1–12.
[34] A. de Juan, J. Jaumot, R. Tauler, *Anal. Methods* **2014**, *6*, 4964–4976.
[35] J. J. Rehr, J. J. Kas, F. D. Vila, M. P. Prange, K. Jorissen, *Phys. Chem. Chem. Phys.* **2010**, *12*, 5503–5513.
[36] a) G. Kresse, J. Furthmüller, *Phys. Rev. B* **1996**, *54*, 11169–11186; b) G. Kresse, J. Furthmüller, *Comput. Mater. Sci.* **1996**, *6*, 15–50.
[37] S. R. Bahn, K. W. Jacobsen, *Comput. Sci. Eng.* **2002**, *4*, 56–66.
[38] a) P. E. Blöchl, *Phys. Rev. B* **1994**, *50*, 17953–17979; b) G. Kresse, D. Joubert, *Phys. Rev. B* **1999**, *59*, 1758–1775.
[39] J. Wellendorff, K. T. Lundgaard, A. Møgelhøj, V. Petzold, D. D. Landis, J. K. Nørskov, T. Bligaard, K. W. Jacobsen, *Phys. Rev. B* **2012**, *85*, 235149 (1–23).
[40] H. J. Monkhorst, J. D. Pack, *Phys. Rev. B* **1976**, *13*, 5188–5192.

Manuscript received: May 11, 2021
Revised manuscript received: July 5, 2021
Accepted manuscript online: July 14, 2021
Version of record online: August 18, 2021